ACS APPLIED MATERIALS & INTERFACES

www.acsami.org

Research Article

# Two-Dimensional Designer Nanochannels for Controllable Ion Transport in Graphene Oxide Nanomembranes with Tunable Sheet Dimensions

Taemin Lee and Byeong-Su Kim*

Cite This: *ACS Appl. Mater. Interfaces* 2020, 12, 13116−13126

Read Online

ACCESS | Metrics & More | Article Recommendations | Supporting Information

**ABSTRACT:** Graphene is a distinct two-dimensional (2D) material that provides a wide range of opportunities for membrane applications owing to its ultimate thinness, flexibility, chemical stability, and mechanical strength. In particular, chemically functionalized graphene oxide (GO) sheets containing amine and carboxylic acid groups facilitate solution-based processing and the formation of various internal structures depending on their properties such as the lateral dimension, defect density, and number of stacked layers. In this study, we designed and fabricated a multilayered GO membrane via the layer-by-layer assembly of two oppositely charged GO nanosheets and investigated the effects of the (1) lateral dimension of the GO nanosheet and (2) membrane thickness of the 2D nanochannels of the GO membrane on the ion permeation behavior. The correlations between the structural parameters of the GO membranes and ion diffusion kinetics were evaluated using the Nielsen model. The functional groups were selectively ionized by exposure to pH-adjusted water, which creates positive or negative net charges, resulting in an ion-selective permeability. The unique properties of the GO nanosheets play important roles in determining the trade-off between the membrane permeability and selectivity, leading to new applications of GO nanosheets as functional membranes.

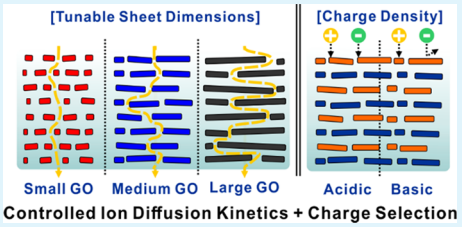


**KEYWORDS:** *graphene oxide membrane, layer-by-layer assembly, sheet dimension, ionic permeability, pH-switchable selectivity*

## 1. INTRODUCTION

The design of microporous membranes is essential for industrial applications such as water purification and desalination, sensing, and energy conversion.[1−3] Microporous membranes have an open and random structure consisting of highly interconnected pores, similar to that of a conventional filter in terms of the structure and function. However, these pores are extremely small (1 to 100 nm in diameter) compared with those of conventional filters, leading to an exceptional separation capability at the molecular level based on size exclusion, chemical interactions, and diffusion kinetics.[4,5]

With the development of two-dimensional (2D) materials, the assembly of these 2D materials offers extraordinary physicochemical properties[6−8] that are being exploited in a growing range of applications in electronics, photonics, energy conversion and storage, and biomedical technologies. In particular, the use of 2D building blocks such as graphene and graphene oxide (GO),[9−13] zeolite,[14] and metal−organic framework nanosheets[15,16] in membrane design allows the formation of an ultrathin separating layer that can selectively filtrate the molecules or ions. Among them, GO nanosheets have received great attention due to their excellent molecular sieving capabilities and fast permeation kinetics.[17−21] Especially, owing to their excellent thermal and mechanical properties with a high aspect ratio, the stacking of GO nanosheets provides the well-defined carbon nanochannels for water purification that allow the flow of a water fluid while rejecting the contaminants. Moreover, the presence of abundant oxygen-containing groups on GO nanosheets can facilitate surface modification of membranes with desired functional groups. In a pioneering work, Geim and co-workers demonstrated that submicrometer-thick GO membranes allow the unimpeded permeation of water, while other small molecules cannot penetrate the closely spaced graphene sheets.[10] Another advantage of 2D GO nanosheets is their structural tunability with respect to the membrane thickness, pore size, and pore distribution, which results in a well-defined permeation behavior with an outstanding molecular selectivity. Similarly, Park and co-workers achieved selective gas diffusion in few-layered graphene-coated polymer membranes by controlling the number of graphene layers, which affects the gas flow channels and pores.[22] Thus, 2D graphene sheets are considered to be a suitable building block for microporous

Received: November 10, 2019
Accepted: February 23, 2020
Published: February 24, 2020






https://dx.doi.org/10.1021/acsami.9b20398
*ACS Appl. Mater. Interfaces* 2020, 12, 13116−13126

**Scheme 1. Schematic of Multilayered GO Membranes Designed for Controllable Ion Permeation Based on the Variation of the Sheet Size and Membrane Thickness**

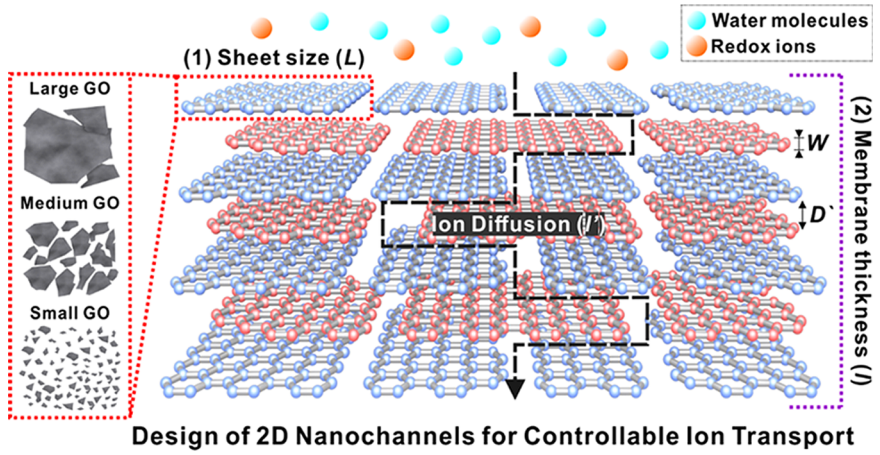


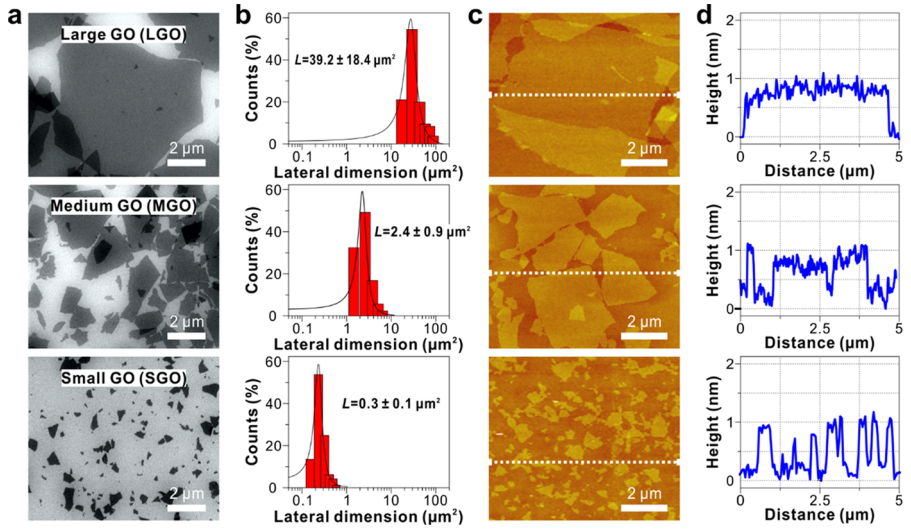


**Figure 1.** (a) SEM images of the three types of GO sheets and (b) histograms of their size distributions. Depending on the average lateral dimension, GO sheets with varying dimensions were defined as LGO, MGO, and SGO. The histograms were obtained by counting more than 200 sheets for each sample. (c) Representative AFM images of the three different GO sheets and (d) corresponding height profiles.

membrane applications because of their inherent transport behavior at the molecular scale.

Graphene-based membranes are commonly fabricated using hierarchical bottom-up approaches such as vacuum-assisted filtration,[23−26] the Langmuir−Blodgett technique,[27,28] and layer-by-layer (LbL) assembly,[29−31] which integrates the 2D graphene into a layered architecture through nanoscale interfacial engineering. However, graphene-based membranes prepared by filtration and the Langmuir−Blodgett technique often lack interaction between the graphene layers due to the hydrophilicity of the GO nanosheets, which makes them to be easily peeled off from the surface or disintegrate when facing common environmental changes. Moreover, there are limitations in controlling the internal structure of the membrane such as the pore size, composition, and thickness. On the other hand, the LbL assembly allows the fine-tuning of the film thickness, composition, and desired properties depending on the choice of the layering materials and deposition conditions.[32−36] The LbL assembly can be driven by various molecular interactions between each component, including electrostatic interaction, hydrogen bonding, charge transfer interactions, and covalent bonding, which provide a stable interlayer attraction between each graphene sheet.[37−39]

The presence of abundant oxygen functional groups on the GO surface not only facilitates the dispersion in polar solvents but also provides handles for surface modification of the membranes and charge-based separation, similar to conventional weak polyelectrolytes.[40−42] In our previous work, we investigated the pH-responsive behavior of GO membranes by varying the charge density of GO nanosheets during LbL growth; the membranes exhibited a selective permeation in response to the external pH.[43] However, because the permeation performance in relation to the structural geometry of the GO membrane has not been fully discussed thus far, in this study, we aim to investigate the permeation behavior and diffusion kinetics through 2D nanochannels within the GO membrane depending on the size of the GO blocks ($L$) and membrane thickness ($l$) (Scheme 1). In particular, the size-variable GO nanosheets can provide the differences in the defect density, aspect ratio, and charge density (i.e., density of ionizable functional groups). Therefore, it is anticipated that the size of GO blocks will affect the key membrane properties



https://dx.doi.org/10.1021/acsami.9b20398
ACS Appl. Mater. Interfaces 2020, 12, 13116−13126

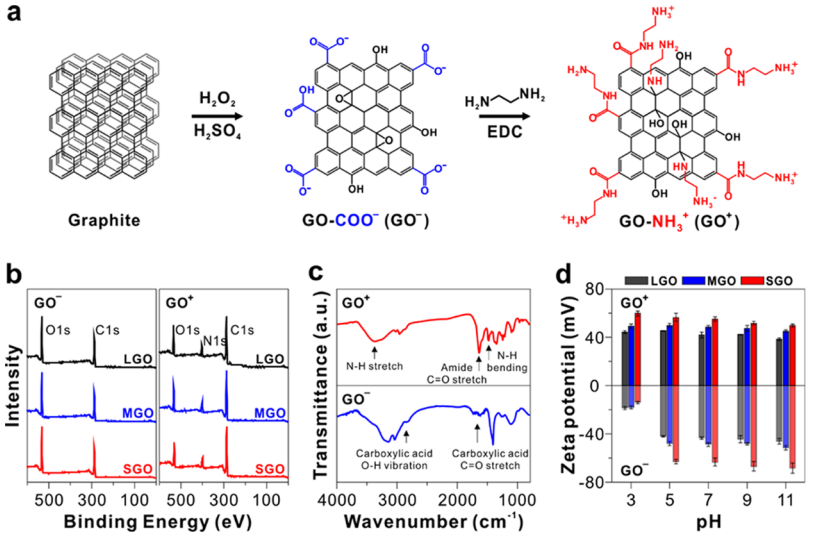


**Figure 2.** (a) Schematic of amine functionalization of chemically exfoliated GO sheets. (b) XPS profiles of the $GO^-$ and $GO^+$ sheets, (c) FT-IR spectra of the LGO sheets, and (d) zeta potentials of functionalized GO sheets with different lateral dimensions at various pH values.

such as the surface porosity, diffusion kinetics, permeation flux, and selectivity of molecules or ions.

Multilayered GO membranes were fabricated using the LbL assembly by exploiting oppositely charged functionalized GO blocks. We systematically investigated the ion transport behavior using electrochemical analyses with charged redox molecules. In addition, the pH-induced ionic permselectivity of the GO membranes was explored by taking advantage of ionizable side groups of the functionalized GO blocks such as carboxyl acid and amine groups. The functionalized GO membrane possesses an excess positive or negative net charge depending on the external pH, resulting in an ion permselectivity depending on the charge density. We anticipate that this study will open possibilities for new applications of GO sheets in various membranes.

## 2. RESULTS AND DISCUSSION

**2.1. Characterization of Size-Controlled GO Sheets.** The physicochemical properties of the assembled GO membranes are largely determined by the characteristics of the constituent GO blocks.[44−46] For example, a large-sized GO sheet is likely to form a mechanically stable and robust membrane structure due to the high density of the interconnected graphene sheets based on van der Waals interactions. On the other hand, a small-sized GO sheet has abundant charged functional groups on the surface, which facilitate strong electrostatic interactions. Therefore, the structural diversity of GOs derived from their chemical compositions, lateral dimensions, and lattice defects is a critical factor in determining the membrane performance of multilayered GO membranes.

Several approaches can be used to obtain high-quality graphene sheets with uniform size distributions such as pH-assisted selective sedimentation,[47] density gradient ultracentrifugation,[48,49] and the tuning of the chemical oxidation degree.[50−52] However, these approaches have limitations in terms of the mass production and the size homogeneity. In this study, we adopted a unique method to adjust the fracture densities of the graphene structures by applying mechanical stimuli such as high shear force and ultrasonic treatments (Figure 1). Based on a mechanical force induced by shear stress, large-sized graphene sheets with few defects form due to the mild exfoliation process, while ultrasonic processing causes significant disruptions in the weak chemical bonds, resulting in extremely small and highly defective GO nanosheets.

As shown in the scanning electron microscopy (SEM) images, graphene sheets with three different sizes were synthesized using different exfoliation processes. The sizes are uniformly distributed, and the lateral dimensions range from several micrometers to several nanometers (Figure 1b). Depending on the average lateral dimension, we classified the graphene sheets as large-sized GO (LGO, average dimension of 39.2 ± 18.4 $\mu m^2$), medium-sized GO (MGO, average dimension of 2.4 ± 0.9 $\mu m^2$), and small-sized GO (SGO, average dimension of 0.3 ± 0.1 $\mu m^2$). The representative atomic force microscopy (AFM) images indicate that the obtained GO sheets were successfully exfoliated into a single-layer GO sheet with a thickness of ∼1 nm (Figure 1c,d).

**2.2. Synthesis of Amine-Functionalized GO Sheets.** The multilayered GO membranes were fabricated by using the successive adsorption of oppositely charged GO building blocks based on electrostatic attraction. The chemically exfoliated GO sheets display a stable colloidal dispersity in aqueous media due to the presence of many oxygen-containing functional groups that were introduced during the chemical oxidation process.[53] In particular, the carboxylic acid group imparts intrinsically strong negative charges (GO−$COO^-$; $GO^-$ hereafter) to the graphene sheets over a wide range of pH conditions. The presence of oxygen functional groups facilitates chemical functionalization. Subsequently, positively charged graphene sheets (GO−$NH_3^+$; $GO^+$ hereafter) were prepared by introducing amine groups based on the *N*-ethyl-*N*′-(3-dimethylaminopropyl)carbodiimide methiodide (EDC)-mediated coupling reaction between the carboxylic acids and excess ethylenediamine as demonstrated in our previous report (Figure 2a).[54]

To demonstrate the successful functionalization, X-ray photoemission spectroscopy (XPS) and Fourier transform infrared (FT-IR) spectroscopy were used. The XPS profiles confirm the presence of amine-bearing groups in the functionalized $GO^+$ sheets; a distinctly evolving nitrogen peak (∼7.6 atom %) is detected, which is absent in pristine


https://dx.doi.org/10.1021/acsami.9b20398
ACS Appl. Mater. Interfaces 2020, 12, 13116−13126

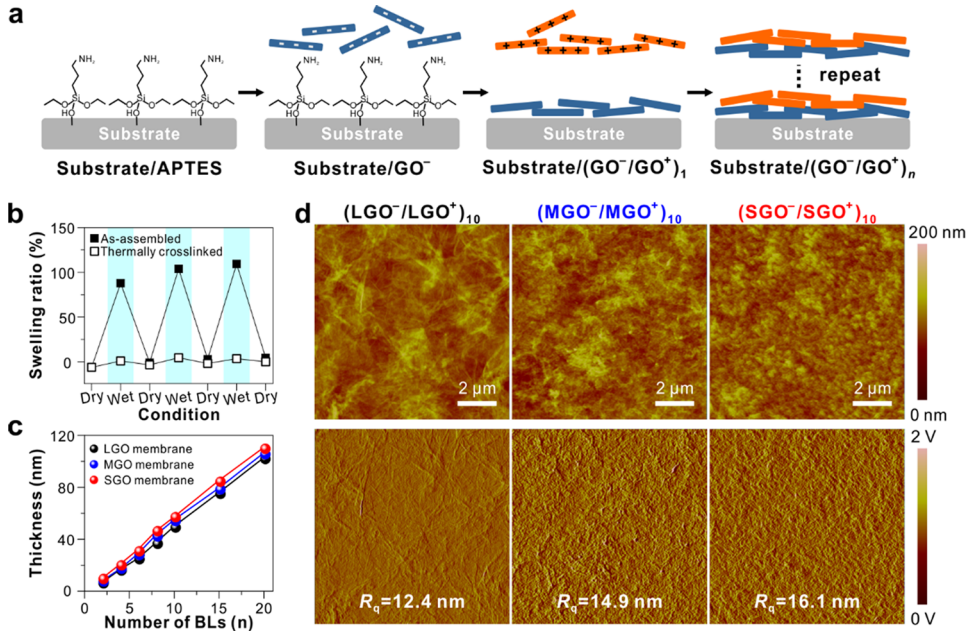


**Figure 3.** (a) Illustration of the GO membrane fabrication by LbL assembly based on electrostatic interactions between the $GO^-$ and $GO^+$ sheets. (b) In situ ellipsometric thickness changes of 10-BL LGO films in dry and wet environments before and after thermal cross-linking. (c) Ellipsometric thickness profiles of the assembled GO membranes as a function of the number of BLs. (d) Representative AFM images of the three types of multilayered graphene membranes. Each film was assembled on a silicon wafer, and the morphology and surface roughness were characterized using the 10-BL samples.

$GO^-$ sheets (Figure 2b). In addition, the C/O atomic ratio increases from 1.8 ($GO^-$) to 3.7 ($GO^+$) upon functionalization, while the oxygen level slightly increases with decreasing GO sheet dimension (Table S1). This indicates that the oxidation level of the GO sheets is significantly affected by the structural difference induced by the number of defects within the GO sheets. The high-resolution C 1s spectra indicate the presence of $sp^2/sp^3$ C, C−O, and C═O peaks in the pristine $GO^-$ sheets; an additional C−N peak can be observed after amine functionalization (Figure S1 and Table S2). The FT-IR spectrum of $GO^-$ shows abundant hydroxyl, carboxyl, and epoxide groups as indicated by characteristic peaks of the C−H stretching vibration at 3100 and 3000 $cm^{-1}$, C═O stretching vibration at 1735 $cm^{-1}$, C═C stretching vibration at 1620 $cm^{-1}$, O−H vibration at 1406 $cm^{-1}$, and C−O stretching vibration at 1100 $cm^{-1}$ (Figure 2c). In the $GO^+$ sheet, new vibration bands emerge at ∼1639 and 1483 $cm^{-1}$, corresponding to the C═O stretching and N−H bending vibrations of the primary amide, whereas the bands of the carboxylic group at 1735 and 1225 $cm^{-1}$ are not observed in the $GO^-$ spectrum after amine functionalization. These results indicate the covalent attachment of ethylenediamine to the GO surface through the formation of an amide bond. The surface zeta potential of the functionalized GO suspension reveals the surface charge characteristics of each GO sheet, clearly demonstrating the charge reversal from negative (from −70 to −20 mV) to positive surface charges (from +40 to +60 mV; Figure 2d). Furthermore, we observed a change in the degree of ionization of each GO sheet when the pH was adjusted from 3 to 11, which is due to the presence of carboxyl and amine groups; this is similar to the pH-tailored behavior of typical weak polyelectrolytes. Interestingly, the smaller-sized SGO possessed a higher zeta potential than the other GO sheets with larger lateral dimensions, which indirectly indicates the difference in the density of the reactive functional groups depending on the sheet dimensions. Thus, the adjustment of the GO dimension can alter the degree of ionization of the GO suspension and consequently lead to differences in the thickness and morphology of the resulting LbL-assembled GO membranes.

**2.3. Fabrication of the GO Membrane via LbL Assembly.** By using oppositely charged GO suspensions, the multilayered GO thin membranes were fabricated on a silicon wafer or indium−tin oxide (ITO) electrode through LbL assembly. The layer composition of the resulting GO films is significantly influenced by the pH value of each GO solution because of the different charge densities, which depend on the degree of protonation. Thus, we fixed the pH of both GO suspensions at 3.0 during the LbL growth to reduce the effect of the pH on the structure of the GO multilayer membranes.

The design of the internal morphology of the assembled GO membranes is based on two factors: (1) the lateral size of the GO building block and (2) the membrane thickness based on the number of LbL assembly. Before the assembly, the substrate was treated with (3-aminopropyl)triethoxysilane (APTES) solution to render the positively charged surface.[55] After the APTES treatment, the positively charged substrate was dipped into a negatively charged $GO^-$ solution (0.50 mg/mL, pH 3.0) for 10 min, leading to the adsorption of one monolayer and reversal of the surface charge. Subsequently, the substrate was rinsed with distilled water at the same pH to remove loosely adsorbed $GO^-$ sheets. The $GO^-$-coated substrate was dipped in a positively charged $GO^+$ solution (0.50 mg/mL, pH 3.0) for 10 min followed by a rinsing step. Finally, we obtained a one-bilayer (BL) $(GO^-/GO^+)_1$ film. These procedures were repeated to achieve the desired number of BLs. The notation of each GO membrane prepared is presented as "$(xGO^-/xGO^+)_n$" based on the size of GO blocks ($x$ = LGO, MGO, and SGO) and the number of BLs ($n$; Figure 3a). To enhance the mechanical integrity and diminish


https://dx.doi.org/10.1021/acsami.9b20398
ACS Appl. Mater. Interfaces 2020, 12, 13116−13126

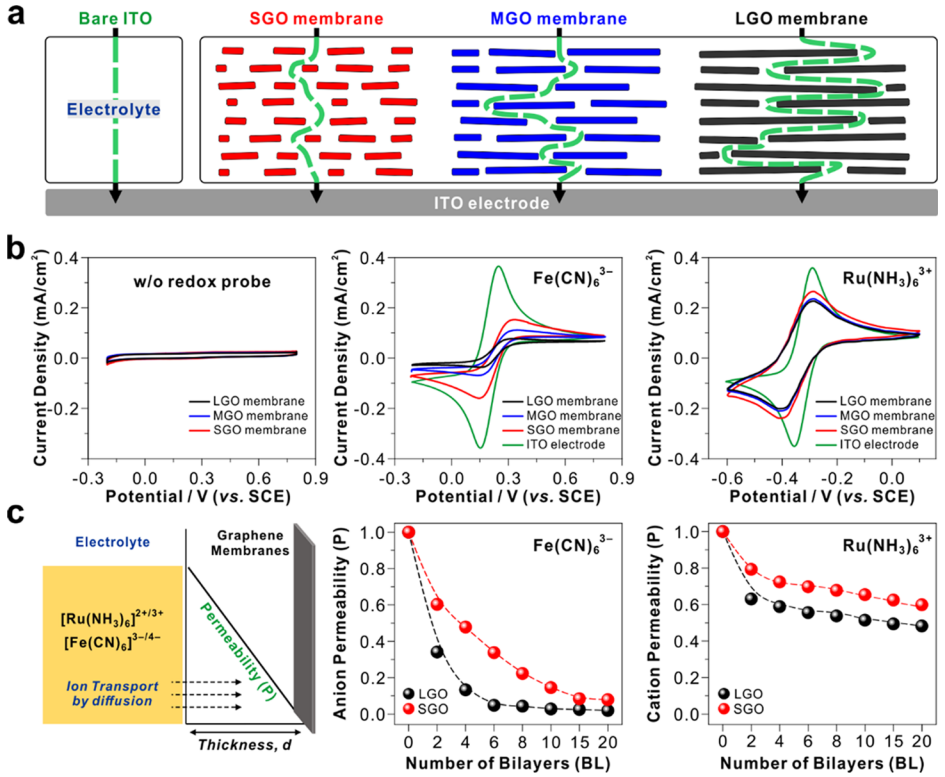


**Figure 4.** (a) Schematic representation of the ion transport through multilayered GO membranes with differently sized GO building blocks. The green arrow indicates the expected diffusion length ($l'$) of the redox ions in the GO multilayer membranes. (b) Comparison of the voltammetric responses of the LGO, MGO, and SGO membranes (10 BL) in the absence and presence of anionic and cationic redox probes, $Fe(CN)_6^{3-}$ and $Ru(NH_3)_6^{3+}$, respectively. (c) Relative anion and cation permeability of the LGO and SGO membranes depending on the number of BLs (0 to 20 BL). The permeability was calculated based on the ITO electrode (for 0 BL) using the Nielsen model, which reflects the ion transport capacity corresponding to the lateral dimensions of the GO sheets and membrane thickness. Three-electrode configurations were employed at a scan rate of 20 mV/s in aqueous 0.50 M $Na_2SO_4$ electrolyte solutions containing 5.0 mM $Fe(CN)_6^{3-}$ or $Ru(NH_3)_6^{3+}$ as the electroactive species.

the swelling of the membranes when they are exposed to aqueous media, the as-assembled GO multilayer membranes were subjected to a thermal treatment in a vacuum oven at 150 °C for 12 h. The results of the in situ ellipsometry demonstrate that the as-assembled GO films swell up to 120% when they are dipped in water in a dry state, while the swelling could be considerably suppressed to less than 15% after thermal cross-linking (Figure 3b and Figure S2). Based on these observations, it can be concluded that the thermal cross-linking of the GO multilayer membranes improves their mechanical stabilities while maintaining the interconnected nanochannels between the graphene interlayers, which are necessary for effective water molecule permeation through the membrane.

Figure 3c shows the uniform growth of the resulting GO multilayers; the film thickness gradually increases from 9.1 to 97.8 nm as the number of BL increases from 2 to 20 BL. The average BL thickness of the LGO, MGO, and SGO films are 4.5, 4.8, and 5.2 nm, respectively. Additionally, the representative cross-sectional transmission electron microscopy (TEM) image exhibits a uniform growth of the multilayered GO nanostructure that is highly oriented parallel to the substrate (Figure S3).

We also observed that the dimensions of the GO sheet affect the surface morphology of the resulting GO multilayer membrane. From the AFM results of the 10-BL GO films [i.e., $(LGO^-/LGO^+)_{10}$, $(MGO^-/MGO^+)_{10}$, and $(SGO^-/SGO^+)_{10}$ membranes], the surface roughness ($R_q$) gradually increases from 12.4 (LGO) to 14.9 (MGO) to 16.1 nm (SGO) (Figure 3d). Accordingly, the LGO sheet has a defect-free, highly uniform, and well-organized structure, while the SGO sheet forms a relatively coarse surface structure composed of many small domains. Based on these results, the morphological design of the internal nanostructure can be varied, clearly demonstrating the benefit of our approach in fabricating highly tunable GO-based membranes by selecting their constituents.

**2.4. Ion Transport Behavior Based on Electrochemical Analysis.** To study the ion transport in the assembled GO membrane, we utilized electrochemical analysis and the anionic and cationic redox molecules of $Fe(CN)_6^{3-}$ and $Ru(NH_3)_6^{3+}$, respectively.[56] Typically, the redox ions quickly access the surfaces of the electrodes, which have small resistances. The redox peak intensity of the voltammetric response is closely related to the transport capabilities of the redox ions through the electrodes. Thus, we fabricated the GO membranes on ITO substrates via LbL assembly and calculated the relative ion permeabilities of the GO membranes using the redox peak current ($i_p$) of the bare ITO electrode (without GO membrane).[57,58]

First, we determined the effect of the size of the graphene block on the ion transport behavior. The number of BLs of the assembled GO membrane was fixed to 10 BL (thickness of ~60 nm). Based on the abovementioned structural analysis, we anticipated that the numbers of ion transport channels and flow resistances in the GO membranes vary depending on the sizes of the GO blocks (from LGO to MGO and to SGO)


https://dx.doi.org/10.1021/acsami.9b20398
ACS Appl. Mater. Interfaces 2020, 12, 13116−13126

(Figure 4a). A simple permeability model for a regular arrangement of two-dimensional platelets was proposed by Nielsen for the case in which the molecules pass through the layered structure in the perpendicular direction.[59,60] All GO blocks within a multilayered GO membrane prepared in this study are presumed to be rectangular in shape and oriented perpendicular to the direction of ion diffusion. Therefore, the ion diffusion path length in these 2D-layered structures can be maximized, which significantly decreases the ion flux through the layered membranes. The diffusion length ($l'$) can be estimated using eqs 1 and 2[61]

$$l' = l + \langle N \rangle \frac{L}{2} \tag{1}$$

$$\langle N \rangle = \frac{l}{D' + W} \tag{2}$$

where $l$ is the membrane thickness, $L$ is the width of the graphene sheet, $N$ is the number of stacked graphene layers, $D'$ (~1.2 nm for hydrated GO sheets) is the interlayer spacing between the graphene sheets,[62] and $W$ is the thickness of the GO sheet (~1 nm). The diffusion path length of the multilayered GO membrane is significantly influenced by the size of the GO blocks. The diffusional path of a large LGO block with an average lateral dimension of 5 $\mu m^2$ is 1800 times longer than the membrane thickness. On the other hand, the diffusion path of a small SGO block with a size of 0.2 $\mu m^2$ is only 40 times longer than the membrane thickness.

As shown in Figure 4b, in the absence of a redox probe, the GO membranes do not exhibit any redox reaction without the appearance of distinct redox peaks. On the other hand, the redox activity based on the presence of anionic and cationic probes on the bare ITO electrode is almost reversible, indicated by a significantly large peak current ($i_p$) of 0.38 mA/cm$^2$ and a small peak separation ($\Delta E_p$) of 65 mV (Figure S4). However, when a multilayered GO membrane is present on the surface of the ITO electrode, the voltammetric response sharply decreases and the peak separation ($\Delta E_p$) becomes large (150 mV). The relative peak current density of $Fe(CN)_6^{3-}$ (considering bare ITO as 100%) decreases to 28, 16, and 10% in the SGO, MGO, and LGO membranes, respectively. In the case of $Ru(NH_3)_6^{3+}$, a similar decrease can be observed, but the difference is not as large as it is observed in the anionic redox probe. We postulate that the assembled GO membrane has a strong negative net charge at a neutral electrolyte pH because the ionized carboxylic acid groups on the edges of the GO sheets are more dominant than the amine groups among the entire functional groups of the GO multilayers. Overall, the GO membrane serves as a barrier against ion diffusion, which impedes the fast penetration of redox molecules to the surface of the ITO electrode.

We further explored the effects of the sheet size and membrane thickness on the redox ion permeability of the membrane depending on the increase in the number of BLs. The Nielsen model, which assumes an almost perfect arrangement of clay particles, has been widely accepted and fits the experimental observations well in several cases, especially with respect to small volume fractions ($\varphi < 0.1$). The correlations between the structural parameters of the GO multilayer membranes, such as the sheet size and thickness and ion diffusion kinetics can be estimated using the Nielsen model expressed in eqs 3 and 4[63−65]

$$\frac{D_0}{D} = \tau = 1 + \frac{L}{2W}\Phi \tag{3}$$

$$\frac{P}{P_0} = \frac{1 - \Phi}{1 + \frac{\alpha}{2}\Phi} \tag{4}$$

where $D$ is the diffusion coefficient of the redox molecules; $\tau$, $\Phi$, and $P$ are the tortuosity, internal volume fraction, and relative permeability of the GO membranes (vs. the bare ITO electrode), respectively; $D_0$ and $l_0$ are the references for bare ITO electrodes; and $\alpha$ (= $L/W$) is the aspect ratio of the GO sheets used (5000 and 200 for LGO and SGO, respectively). The relative diffusion coefficient of each GO multilayer can be obtained from the voltammetric response by using the Randles−Sevcik equation expressed in eq 5[66]

$$i_p = 0.4463nFAC\left(\frac{nFvD}{RT}\right)^{1/2} = 2.69 \times 10^5 n^{3/2} A D^{1/2} C v^{1/2} \tag{5}$$

where $i_p$, $n$, $A$, $D$, $C$, and $v$ are the peak current, number of transferred electrons ($n$ = 1, in this study), electrode area (cm$^2$), diffusion coefficient (cm$^2$/s), concentration of the redox probe (mol/cm$^3$), and scan rate (V/s), respectively. Based on the voltammetric response with the increase in the scan rate from 20 to 200 mV/s, the diffusion coefficient ($D_0$) of the redox probe was calculated to be 3.91 and 3.52 for $Fe(CN)_6^{3-}$ and $Ru(NH_3)_6^{3+}$, respectively. These values gradually decrease as the number of BL increases as summarized in Figure S5 and Table S3. Using the calculated diffusion coefficient ($D/D_0$) of each GO membrane, we evaluated the correlations between the relative anionic or cationic permeability and the different GO blocks and membrane thickness as represented in Figure 4c.

Because the permeability is inversely proportional to the membrane thickness due to the prolonged transport pathway with increased permeation resistance, the electrochemical activity of the redox molecules containing anions and cations steadily decreases when the number of BLs increases from 2 to 20 BL and almost disappears at 20 BL. This observation suggests that the redox molecules cannot penetrate through thick GO membranes with 20 BL (approximately 100 nm thick) (Figure S6). In terms of sizes of the GO blocks, it is believed that a compact and dense structure of the $(LGO^-/LGO^+)_{10}$ membrane derived from large LGO sheets spontaneously lowers the permeation efficiency and diffusion kinetics of the redox molecules. Therefore, the suppression of the ionic permeability of the LGO membranes increases with the increasing number of BLs compared with that of SGO membranes. These results support the fact that the sizes of the building blocks play critical roles in controlling the densities of the 2D nanochannels that are used for ion transport in multilayered architectures.

Furthermore, it should be noted that each redox species has a different sensitivity, that is, the anionic probe does not easily penetrate the GO membrane, while the cationic probe is highly permeable regardless of the lateral size of the GO block. In our previous studies, we assembled multilayered GO membranes with two different outermost layers, for example, 10-BL ($GO^+$ outermost layer) and 10.5-BL ($GO^-$ outermost layer) membranes. Interestingly, the different surface charges of the outermost layers did not lead to noticeable differences in the electrochemical behaviors of redox probes. Thus, we assume


https://dx.doi.org/10.1021/acsami.9b20398
ACS Appl. Mater. Interfaces 2020, 12, 13116−13126

that the overall net charge of the GO multilayers, which depends on the assembly conditions and external pH, is a more important factor in controlling the ion-selective transport behavior than the outermost surface charge.

**2.5. pH-Triggered Molecular Filtration Performance.** Stimuli-responsive materials have great potential as a membrane because they allow the fine-tuning of the separation performance in response to environmental changes such as pH, temperature, and light and offer a significant advantage over conventional membranes. In fact, polymeric membranes with pH-responsive functional groups exhibit improved separation performances and selective chemical sensing based on the control of the net charges of the membrane.[67,68] Owing to the presence of pH-reactive functional groups of GO sheets, such as carboxylic acid and amine groups, the pH-dependent behavior will be translated into the GO membrane assembled from GO sheets. For example, the GO membrane is highly positively charged in acidic electrolytes because of the protonation of amine groups, whereas it is negatively charged in alkaline electrolytes because of the deprotonation of carboxylic acid groups. Because of this protonation/deprotonation equilibrium, the charge properties of the GO membranes can be controlled by external pH conditions.

First, the pH-induced permeation characteristics of GO membranes were examined using the charged redox probes in an acidic or alkaline environment (Figure 5a). The changes in the voltammetric response of GO membranes reflect the difference in the specific probe diffusion because of the net charges of the membranes. At pH 3, there was no selectivity for specific charges, and the peak intensity was nearly constant for both anions and cations, indicating the absence of the electrostatic interaction between the GO membrane and charged ions. On the contrary, as the pH increased to 11, the peak intensity of $Ru(NH_3)_6^{3+}$ was almost unchanged, while the redox peak of $Fe(CN)_6^{3-}$ rapidly diminished (Figure 5b). This observation reveals that the fully protonated pores within the membrane behave as an open gate enabling the free diffusion of anionic and cationic species through the GO membrane. When pH is changed from 3 to 11, the population of ionized carboxylic acid groups increased, thus giving origin to a charged permselective pore. Because the sizes of both redox probes are almost identical [6.0 Å for $Fe(CN)_6^{3-}$ and 6.2 Å for $Ru(NH_3)_6^{3+}$], the difference in the selective permeation is only influenced by the net charge of the multilayer membrane but not by the pore sizes. We postulate that the presence of abundant oxygen-containing functional groups on GO multilayers leads to an overall negatively charged surface. These negative charges, however, is charge-balanced with ionized amine groups under acidic conditions, resulting in the permeation of both cations and anions (Figure 5c). It is also observed in the pH-induced swelling test of the GO membrane. Owing to the ionizable carboxylate groups, the thickness of the GO membrane increased significantly when exposed to alkaline conditions ($\Delta l/l_0 \approx 25\%$) compared to acidic conditions ($\Delta l/l_0 \approx 12\%$).

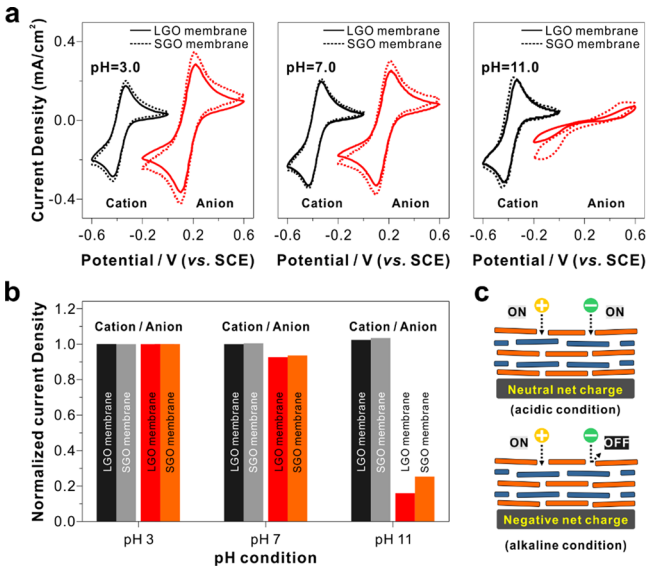


**Figure 5.** (a) Cyclic voltammograms of the multilayered GO membranes in aqueous 0.50 M $Na_2SO_4$ electrolyte solutions containing 5.0 mM $Fe(CN)_6^{3-}$ or $Ru(NH_3)_6^{3+}$ buffered at pH 3.0 and 11.0 and unbuffered at pH 7.0. (b) Histograms showing the changes of the voltammetric response arising from the influence of pH and sheet size on the molecular transport of charged redox probes. (c) Schematic representation of the ionic transport processes taking place in the multilayered GO membrane under different pH conditions.

We further investigated the permselectivity of GO membranes using a colored feed solution containing organic dyes of different charges, including cationic dyes (i.e., methylene blue (MB) and rhodamine B (RB)), neutral dyes (i.e., Nile red (NR) and *p*-nitroaniline (NA)), and anionic dyes (i.e., Congo red (CR) and Evans blue (EB)) (Figure 6 and Figure S7). Permeation experiments were performed with a two-cell system separated by the GO membrane. Because it was challenging to obtain a free-standing GO membrane, 10-BL GO membranes were fabricated onto a commercial poly(vinylidene fluoride) (PVDF; 0.45 $\mu$m pore size) membrane as a porous support (Figure S8). The feed solution (0.10 mg/mL) was in contact with the GO multilayers, and the permeance and dye rejection capacity were monitored using UV−vis spectroscopy (Table S4). In principle, when the feed solution is filtered through the GO membrane driven by the applied pressure, the ionic functional groups on GO sheets will interact electrostatically with the charged ions to separate them.

The rejection capacity of dyes was strongly affected by solution pH. In acidic conditions, the intensity of absorption spectra of different charged dye molecules sharply decreased with a rejection rate of up to 90% as observed in Figure 6a. In contrast, in alkaline conditions, the characteristic absorption intensity of these dyes was also significantly decreased, and we could clearly observe the selectivity for specific charges with distinct dye rejection capacity, consistent with the results from electrochemical voltammetric analysis (Figure 6b). Due to the strong electrostatic repulsion between the negatively charged pores and dye molecules, it will interfere with the diffusion behavior of anionic dye molecules entering the pore channels of the GO membrane. As for neutral dye molecules, the electrostatic interaction between the dye and GO membrane is very weak. Hence, the rejection efficiency is mainly attributed to the molecular-size sieving effect. Indeed, the rejection capacity for the neutral dye is almost constant regardless of pH conditions (Figure 6c). These findings indicate that both molecular sieving (sieving effect) and electrostatic repulsion (charge effect) by ionized functional groups on GO sheets dominate the separation process. This unique unipolar sieving effect of multilayered GO membranes could be utilized in the development of charge-based separation processes.


https://dx.doi.org/10.1021/acsami.9b20398
ACS Appl. Mater. Interfaces 2020, 12, 13116−13126

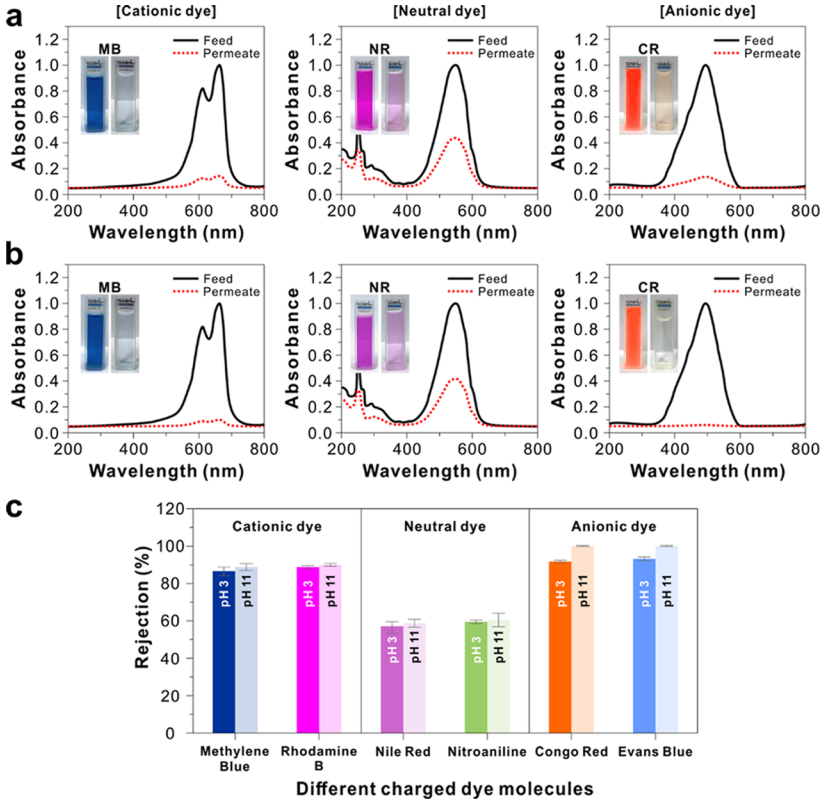


**Figure 6.** UV−vis absorption spectra of different charged dye molecules before and after filtration through an LGO membrane in (a) acidic and (b) alkaline conditions; insets show the photographs of the feed and permeate of the corresponding methylene blue (MB), Nile red (NR), and Congo red (CR) solution. (c) Rejection capacity of the different charged dye molecules during the filtration through LGO multilayers assembled on a PVDF membrane under different pH conditions.

## 3. CONCLUSIONS

We demonstrate the assembly of multilayered GO membranes based on the LbL approach, which allows the precise control of many critical membrane parameters, including the thickness, morphology, charge density, and internal structures, which are hard to control with other conventional techniques. We clearly observed that the ion transport through the unique 2D nanochannels can be fine-tuned by controlling two engineering factors, that is, the lateral size of the GO building block and membrane thickness. In addition, we confirmed that the GO membranes have different charge densities due to the presence of ionizable side groups such as amine and carboxylic acid groups. These functional groups are selectively ionized depending on the pH of the solution. Therefore, the GO membranes exhibit an anion-selective behavior.

The 2D graphene sheets are suitable for microporous membrane applications because of their unique transport behavior at the molecular scale. Their high impermeability and permselectivity are of great advantage and may lead to many novel applications for which conventional techniques are not suitable. Our LbL assembly approach to the fabrication of GO membranes is valuable for the design of graphene-based membranes with desired properties and provides guidance for fundamental research in materials science, chemical engineering, and membrane technology. Considering the recent surge of interest in the development of membrane technology, this study provides valuable insights into the fundamental properties and possibilities of 2D polyelectrolyte-based multilayers in novel functional membranes.

## 4. EXPERIMENTAL SECTION

**4.1. Preparation of GO Sheets with Varying Dimensions.** Graphite oxide was synthesized using a modified Hummers' method and then exfoliated using different exfoliation processes to yield GO suspensions with varying dimensions.[69−72] First, dried graphite oxide powder (50 mg) was dispersed in 100 mL of deionized (DI) water and exfoliated using a homogenizer for 30 min to obtain large-sized GO (LGO) sheets. Subsequently, LGO sheets were sonicated again for 30 min at different intensities of 100 and 300 W to obtain medium-sized GO (MGO) and small-sized GO (SGO) sheets, respectively.

**4.2. Preparation of Amine-Functionalized GO Sheets.** The resultant GO was negatively charged over a wide range of pH conditions. To introduce amine groups ($-NH_2$) to the as-prepared GO sheets, a 100 mL GO suspension (conc. of 0.50 mg/mL) was reacted with 1.25 g of *N*-ethyl-*N*′-(3-dimethylaminopropyl)-carbodiimide methiodide (EDC) and 10 mL of ethylenediamine for 12 h and then subjected to dialysis (MWCO 12000-14000, Spectra/Por dialysis membrane) for three days to remove excess residual chemicals and byproducts.[54,73]

**4.3. Layer-by-Layer Assembly of Multilayered GO Membranes.** Before the assembly, silicon wafer or ITO substrates were thoroughly cleaned to remove any organic contamination and treated with (3-aminopropyl)triethoxysilane (APTES) solution (10% v/v in ethanol) for 6 h to render the positively charged surface. After the APTES treatment, the substrate was thoroughly washed with ethanol to remove weakly bound excess residual molecules from the surface. The positively charged substrate was dipped into a negatively charged $GO^-$ solution (0.50 mg/mL, pH 3.0) for 10 min, leading to the adsorption of one monolayer and to the reversal of the surface charge. The substrate was then rinsed three times with distilled water at the same pH for 1 min to remove the loosely adsorbed $GO^-$ from the substrate. Then, the substrate was coated with a positively charged


https://dx.doi.org/10.1021/acsami.9b20398
ACS Appl. Mater. Interfaces 2020, 12, 13116−13126

GO solution (0.50 mg/mL, pH 3.0) followed by a rinsing step. We then obtained a one-bilayer (BL) $(GO^-/GO^+)_1$ membrane. The abovementioned procedures were repeated to achieve the desired number of BLs. Subsequently, the as-assembled GO multilayer films were subjected to thermal cross-linking in a vacuum oven at 150 °C for 12 h to prevent the degradation of the film structure by swelling in an aqueous solution.

**4.4. Characterization of the Multilayered GO Membranes.** The thickness of the multilayered graphene films on the silicon substrate was measured using ellipsometry (J. A. Woollam Co., USA, EC-400 and M-2000V). The average thickness values were calculated using three individual measurements. The AFM images of the multilayered graphene films were used to determine the surface morphology and roughness (tapping mode; Veeco, Nanoscope V).

**4.5. Electrochemical Characterization.** Cyclic voltammetry measurements were performed using a VMP3 potentiostat with a three-electrode cell. A platinum wire was used as a counter electrode and a saturated calomel electrode (SCE) was utilized as a reference electrode. Aqueous solutions of 0.5 M $Na_2SO_4$ containing 5 mM of either $Fe(CN)_6^{3-}$ or $Ru(NH_3)_6^{3+}$ buffered at pH 3 and 11 and unbuffered at pH 7 were prepared as electrolyte solutions. To determine the current density, the measured current was divided by the area of the sample that was immersed in solution.

**4.6. Separation Performances of the GO Membranes.** The separation performances of the GO membranes below 0.1 MPa were estimated using organic dyes. The initial concentration of the dye solution was set to 0.10 mg/mL. The change of the dye concentration before and after filtration was measured using a UV−vis spectrometer (JASCO V-750). To investigate the effect of the pH on the separation performance of the GO membrane, the initial pH of the feeding solution was adjusted to 3 and 11 by adding 0.1 M HCl or NaOH solutions, respectively.

The permeance, $J$ (L $m^{-2}$ $h^{-1}$ $bar^{-1}$), was measured by collecting the permeate water ($V$) and calculated by the following equation (eq 6)

$$J = \frac{V}{A \times t \times P} \tag{6}$$

where $t$ and $A$ are the operation time and the effective membrane area ($m^2$), respectively. Subsequently, the rejection of the composite membrane with respect to the organic dye was calculated using the following equation (eq 7)

$$R = \left(1 - \frac{C_p}{C_f}\right) \times 100\% \tag{7}$$

where $C_f$ and $C_p$ represent the concentration (mg/mL) of the dye in the feed and permeate in solutions, respectively.

## ■ ASSOCIATED CONTENT

### Supporting Information

The Supporting Information is available free of charge at https://pubs.acs.org/doi/10.1021/acsami.9b20398.

In situ ellipsometric analysis of a GO membrane in dry and wet environments, electrochemical cyclic voltammograms, fitted Randles−Sevcik plots of the GO multilayer membranes, a Table listing the diffusion coefficient and tortuosity calculated for the ITO electrodes deposited with LGO and SGO membrane, and a table of separation performances with different charged dye molecules (PDF)

## ■ AUTHOR INFORMATION


### Corresponding Author

**Byeong-Su Kim** − *Department of Chemistry, Yonsei University, Seoul 03722, Republic of Korea;* orcid.org/0000-0002-6419-3054; Email: bskim19@yonsei.ac.kr

### Author

**Taemin Lee** − *Department of Chemistry, Yonsei University, Seoul 03722, Republic of Korea; Photo-Electronic Hybrids Research Center, Korea Institute of Science and Technology (KIST), Seoul 02792, Republic of Korea*

Complete contact information is available at: https://pubs.acs.org/10.1021/acsami.9b20398


### Notes

The authors declare no competing financial interest.

## ■ ACKNOWLEDGMENTS

This work was supported by the National Research Foundation of Korea (NRF-2017R1A2B3012148 and NRF-2017M3A7B4052802).

## ■ REFERENCES


(1) Elimelech, M.; Phillip, W. A. The Future of Seawater Desalination: Energy, Technology, and the Environment. *Science* **2011**, *333*, 712−717.

(2) Gin, D. L.; Noble, R. D. Designing the Next Generation of Chemical Separation Membranes. *Science* **2011**, *332*, 674−676.

(3) Hegab, H. M.; Zou, L. Graphene Oxide-Assisted Membranes: Fabrication and Potential Applications in Desalination and Water Purification. *J. Membr. Sci.* **2015**, *484*, 95−106.

(4) Reid, C. R.; Thomas, K. M. Adsorption Kinetics and Size Exclusion Properties of Probe Molecules for the Selective Porosity in a Carbon Molecular Sieve Used for Air Separation. *J. Phys. Chem. B* **2001**, *105*, 10619−10629.

(5) Joshi, R. K.; Carbone, P.; Wang, F. C.; Kravets, V. G.; Su, Y.; Grigorieva, I. V.; Wu, H. A.; Geim, A. K.; Nair, R. R. Precise and Ultrafast Molecular Sieving Through Graphene Oxide Membranes. *Science* **2014**, *343*, 752−754.

(6) Frisenda, R.; Navarro-Moratalla, E.; Gant, P.; Pérez De Lara, D.; Jarillo-Herrero, P.; Gorbachev, R. V.; Castellanos-Gomez, A. Recent Progress in the Assembly of Nanodevices and Van der Waals Heterostructures by Deterministic Placement of 2D materials. *Chem. Soc. Rev.* **2018**, *47*, 53−68.

(7) Liu, Y.; Huang, Y.; Duan, X. Van der Waals Integration Before and Beyond Two-Dimensional Materials. *Nature* **2019**, *567*, 323−333.

(8) Kirubasankar, B.; Palanisamy, P.; Arunachalam, S.; Murugadoss, V.; Angaiah, S. 2D MoSe2-Ni(OH)2 Nanohybrid as an Efficient Electrode Material with High Rate Capability for Asymmetric Supercapacitor Applications. *Chem. Eng. J.* **2019**, *355*, 881−890.

(9) Novoselov, K. S.; Geim, A. K.; Morozov, S. V.; Jiang, D.; Zhang, Y.; Dubonos, S. V.; Grigorieva, I. V.; Firsov, A. A. Electric Field Effect in Atomically Thin Carbon Films. *Science* **2004**, *306*, 666−669.

(10) Nair, R. R.; Wu, H. A.; Jayaram, P. N.; Grigorieva, I. V.; Geim, A. K. Unimpeded Permeation of Water Through Helium-Leak−Tight Graphene-Based Membranes. *Science* **2012**, *335*, 442−444.

(11) Ghosh, T.; Biswas, C.; Oh, J.; Arabale, G.; Hwang, T.; Luong, N. D.; Jin, M.; Lee, Y. H.; Nam, J.-D. Solution-Processed Graphite Membrane from Reassembled Graphene Oxide. *Chem. Mater.* **2012**, *24*, 594−599.

(12) Mi, B. Graphene Oxide Membranes for Ionic and Molecular Sieving. *Science* **2014**, *343*, 740−742.

(13) Zheng, Z.; Grünker, R.; Feng, X. Synthetic Two-Dimensional Materials: A New Paradigm of Membranes for Ultimate Separation. *Adv. Mater.* **2016**, *28*, 6529−6545.

(14) Gascon, J.; Kapteijn, F.; Zornoza, B.; Sebastián, V.; Casado, C.; Coronas, J. Practical Approach to Zeolitic Membranes and Coatings: State of the Art, Opportunities, Barriers, and Future Perspectives. *Chem. Mater.* **2012**, *24*, 2829−2844.

(15) Gascon, J.; Kapteijn, F. Metal-Organic Framework Membranes—High Potential, Bright Future? *Angew. Chem., Int. Ed.* **2010**, *49*, 1530−1532.

(16) Shekhah, O.; Liu, J.; Fischer, R. A.; Wöll, C. MOF Thin Films: Existing and Future Applications. *Chem. Soc. Rev.* **2011**, *40*, 1081−1106.
(17) Xi, Y.-H.; Liu, Z.; Ji, J.; Wang, Y.; Faraj, Y.; Zhu, Y.; Xie, R.; Ju, X.-J.; Wang, W.; Lu, X.; Chu, L.-Y. Graphene-Based Membranes with Uniform 2D Nanochannels for Precise Sieving of Mono−/Multi-Valent Metal Ions. *J. Membr. Sci.* **2018**, *550*, 208−218.
(18) Chong, J. Y.; Wang, B.; Mattevi, C.; Li, K. Dynamic Microstructure of Graphene Oxide Membranes and the Permeation Flux. *J. Membr. Sci.* **2018**, *549*, 385−392.
(19) Cho, Y. H.; Kim, H. W.; Lee, H. D.; Shin, J. E.; Yoo, B. M.; Park, H. B. Water and Ion Sorption, Diffusion, and Transport in Graphene Oxide Membranes Revisited. *J. Membr. Sci.* **2017**, *544*, 425−435.
(20) Huang, H.; Ying, Y.; Peng, X. Graphene Oxide Nanosheet: An Emerging Star Material for Novel Separation Membranes. *J. Mater. Chem. A* **2014**, *2*, 13772−13782.
(21) Liu, G.; Jin, W.; Xu, N. Graphene-Based Membranes. *Chem. Soc. Rev.* **2015**, *44*, 5016−5030.
(22) Kim, H. W.; Yoon, H. W.; Yoon, S.-M.; Yoo, B. M.; Ahn, B. K.; Cho, Y. H.; Shin, H. J.; Yang, H.; Paik, U.; Kwon, S.; Choi, J.-Y.; Park, H. B. Selective Gas Transport Through Few-Layered Graphene and Graphene Oxide Membranes. *Science* **2013**, *342*, 91−95.
(23) Dikin, D. A.; Stankovich, S.; Zimney, E. J.; Piner, R. D.; Dommett, G. H. B.; Evmenenko, G.; Nguyen, S. T.; Ruoff, R. S. Preparation and Characterization of Graphene Oxide Paper. *Nature* **2007**, *448*, 457−460.
(24) Putz, K. W.; Compton, O. C.; Segar, C.; An, Z.; Nguyen, S. T.; Brinson, L. C. Evolution of Order During Vacuum-Assisted Self-Assembly of Graphene Oxide Paper and Associated Polymer Nanocomposites. *ACS Nano* **2011**, *5*, 6601−6609.
(25) Tsou, C.-H.; An, Q.-F.; Lo, S.-C.; De Guzman, M.; Hung, W.-S.; Hu, C.-C.; Lee, K.-R.; Lai, J.-Y. Effect of Microstructure of Graphene Oxide Fabricated Through Different Self-Assembly Techniques on 1-Butanol Dehydration. *J. Membr. Sci.* **2015**, *477*, 93−100.
(26) Yang, E.; Ham, M.-H.; Park, H. B.; Kim, C.-M.; Song, J.-H.; Kim, I. S. Tunable Semi-Permeability of Graphene-Based Membranes by Adjusting Reduction Degree of Laminar Graphene Oxide Layer. *J. Membr. Sci.* **2018**, *547*, 73−79.
(27) Cote, L. J.; Kim, F.; Huang, J. Langmuir−Blodgett Assembly of Graphite Oxide Single Layers. *J. Am. Chem. Soc.* **2009**, *131*, 1043−1049.
(28) Mangadlao, J. D.; Santos, C. M.; Felipe, M. J. L.; de Leon, A. C. C.; Rodrigues, D. F.; Advincula, R. C. On the Antibacterial Mechanism of Graphene Oxide (GO) Langmuir−Blodgett Films. *Chem. Commun.* **2015**, *51*, 2886−2889.
(29) Hong, J.; Han, J. Y.; Yoon, H.; Joo, P.; Lee, T.; Seo, E.; Char, K.; Kim, B.-S. Carbon-Based Layer-by-Layer Nanostructures: From Films to Hollow Capsules. *Nanoscale* **2011**, *3*, 4515−4531.
(30) Hu, M.; Mi, B. Enabling Graphene Oxide Nanosheets as Water Separation Membranes. *Environ. Sci. Technol.* **2013**, *47*, 3715−3723.
(31) Heo, J.; Choi, M.; Chang, J.; Ji, D.; Kang, S. W.; Hong, J. Highly Permeable Graphene Oxide/Polyelectrolytes Hybrid Thin Films for Enhanced CO2/N2 Separation Performance. *Sci. Rep.* **2017**, *7*, 456.
(32) Decher, G. Fuzzy Nanoassemblies: Toward Layered Polymeric Multicomposites. *Science* **1997**, *277*, 1232−1237.
(33) Kotov, N. A.; Dékány, I.; Fendler, J. H. Ultrathin Graphite Oxide−Polyelectrolyte Composites Prepared by Self-Assembly: Transition Between Conductive and Non-Conductive States. *Adv. Mater.* **1996**, *8*, 637−641.
(34) Wang, Y.; Angelatos, A. S.; Caruso, F. Template Synthesis of Nanostructured Materials via Layer-by-Layer Assembly. *Chem. Mater.* **2008**, *20*, 848−858.
(35) Yan, Y.; Björnmalm, M.; Caruso, F. Assembly of Layer-by-Layer Particles and Their Interactions with Biological Systems. *Chem. Mater.* **2014**, *26*, 452−460.
(36) Ariga, K.; Yamauchi, Y.; Rydzek, G.; Ji, Q.; Yonamine, Y.; Wu, K. C.-W.; Hill, J. P. Layer-by-layer Nanoarchitectonics: Invention, Innovation, and Evolution. *Chem. Lett.* **2014**, *43*, 36−68.
(37) Sukhishvili, S. A.; Granick, S. Layered, Erasable, Ultrathin Polymer Films. *J. Am. Chem. Soc.* **2000**, *122*, 9550−9551.
(38) Sato, M.; Sano, M. van der Waals Layer-by-Layer Construction of a Carbon Nanotube 2D Network. *Langmuir* **2005**, *21*, 11490−11494.
(39) Kim, B.-S.; Lee, S. W.; Yoon, H.; Strano, M. S.; Shao-Horn, Y.; Hammond, P. T. Pattern Transfer Printing of Multiwalled Carbon Nanotube Multilayers and Application in Biosensors. *Chem. Mater.* **2010**, *22*, 4791−4797.
(40) Whitby, R. L. D.; Korobeinyk, A.; Gun'ko, V. M.; Busquets, R.; Cundy, A. B.; László, K.; Skubiszewska-Zięba, J.; Leboda, R.; Tombacz, E.; Toth, I. Y.; Kovacs, K.; Mikhalovsky, S. V. pH-Driven Physicochemical Conformational Changes of Single-Layer Graphene Oxide. *Chem. Commun.* **2011**, *47*, 9645−9647.
(41) Shih, C.-J.; Lin, S.; Sharma, R.; Strano, M. S.; Blankschtein, D. Understanding the pH-Dependent Behavior of Graphene Oxide Aqueous Solutions: A Comparative Experimental and Molecular Dynamics Simulation Study. *Langmuir* **2012**, *28*, 235−241.
(42) Hu, X.; Yu, Y.; Hou, W.; Zhou, J.; Song, L. Effects of Particle Size and pH Value on the Hydrophilicity of Graphene Oxide. *Appl. Surf. Sci.* **2013**, *273*, 118−121.
(43) Ahn, E.; Gaiji, H.; Kim, T.; Abderrabba, M.; Lee, H.-W.; Kim, B.-S. Graphene Oxide Nanosheet as a Two-Dimensional Polyelectrolyte: pH-Responsive Behavior of a Multilayered Nanomembrane. *J. Membr. Sci.* **2019**, *585*, 191−198.
(44) Loh, K. P.; Bao, Q.; Eda, G.; Chhowalla, M. Graphene Oxide as a Chemically Tunable Platform for Optical Applications. *Nat. Chem.* **2010**, *2*, 1015−1024.
(45) Aba, N. F. D.; Chong, J. Y.; Wang, B.; Mattevi, C.; Li, K. Graphene Oxide Membranes on Ceramic Hollow Fibers − Microstructural Stability and Nanofiltration Performance. *J. Membr. Sci.* **2015**, *484*, 87−94.
(46) Gu, M.; Choi, J.; Lee, T.; Park, M.; Shin, I.-S.; Hong, J.; Lee, H.-W.; Kim, B.-S. Diffusion Controlled Multilayer Electrocatalysts via Graphene Oxide Nanosheets of Varying Sizes. *Nanoscale* **2018**, *10*, 16159−16168.
(47) Wang, X.; Bai, H.; Shi, G. Size Fractionation of Graphene Oxide Sheets by pH-Assisted Selective Sedimentation. *J. Am. Chem. Soc.* **2011**, *133*, 6338−6342.
(48) Green, A. A.; Hersam, M. C. Solution Phase Production of Graphene with Controlled Thickness via Density Differentiation. *Nano Lett.* **2009**, *9*, 4031−4036.
(49) Sun, X.; Luo, D.; Liu, J.; Evans, D. G. Monodisperse Chemically Modified Graphene Obtained by Density Gradient Ultracentrifugal Rate Separation. *ACS Nano* **2010**, *4*, 3381−3389.
(50) Zhang, L.; Liang, J.; Huang, Y.; Ma, Y.; Wang, Y.; Chen, Y. Size-Controlled Synthesis of Graphene Oxide Sheets on a Large Scale Using Chemical Exfoliation. *Carbon* **2009**, *47*, 3365−3368.
(51) Pan, S.; Aksay, I. A. Factors Controlling the Size of Graphene Oxide Sheets Produced via the Graphite Oxide Route. *ACS Nano* **2011**, *5*, 4073−4083.
(52) Zhang, W.; Zou, X.; Li, H.; Hou, J.; Zhao, J.; Lan, J.; Feng, B.; Liu, S. Size Fractionation of Graphene Oxide Sheets by The Polar Solvent-Selective Natural Deposition Method. *RSC Adv.* **2015**, *5*, 146−152.
(53) Park, S.; An, J.; Piner, R. D.; Jung, I.; Yang, D.; Velamakanni, A.; Nguyen, S. T.; Ruoff, R. S. Aqueous Suspension and Characterization of Chemically Modified Graphene Sheets. *Chem. Mater.* **2008**, *20*, 6592−6594.
(54) Ahn, E.; Lee, T.; Gu, M.; Park, M.; Min, S. H.; Kim, B.-S. Layer-by-Layer Assembly for Graphene-Based Multilayer Nanocomposites: The Field Manual. *Chem. Mater.* **2017**, *29*, 69−79.
(55) Kim, J.; Lee, S. W.; Hammond, P. T.; Shao-Horn, Y. Electrostatic Layer-by-Layer Assembled Au Nanoparticle/MWNT Thin Films: Microstructure, Optical Property, and Electrocatalytic Activity for Methanol Oxidation. *Chem. Mater.* **2009**, *21*, 2993−3001.


https://dx.doi.org/10.1021/acsami.9b20398
*ACS Appl. Mater. Interfaces* 2020, 12, 13116−13126

(56) Wang, B.; Anzai, J.-i. Redox Reactions of Ferricyanide Ions in Layer-by-Layer Deposited Polysaccharide Films: A Significant Effect of the Type of Polycation in the Films. *Langmuir* **2007**, *23*, 7378−7384.
(57) Harris, J. J.; Bruening, M. L. Electrochemical and in Situ Ellipsometric Investigation of the Permeability and Stability of Layered Polyelectrolyte Films. *Langmuir* **2000**, *16*, 2006−2013.
(58) Dai, J.; Jensen, A. W.; Mohanty, D. K.; Erndt, J.; Bruening, M. L. Controlling the Permeability of Multilayered Polyelectrolyte Films through Derivatization, Cross-Linking, and Hydrolysis. *Langmuir* **2001**, *17*, 931−937.
(59) Nielsen, L. E. Models for the Permeability of Filled Polymer Systems. *J. Macromol. Sci., Part A: Chem.* **1967**, *1*, 929−942.
(60) Yoo, B. M.; Shin, H. J.; Yoon, H. W.; Park, H. B. Graphene and Graphene Oxide and Their Uses in Barrier Polymers. *J. Appl. Polym. Sci.* **2014**, *131*, 39628.
(61) Choudalakis, G.; Gotsis, A. D. Permeability of Polymer/Clay Nanocomposites: A Review. *Eur. Polym. J.* **2009**, *45*, 967−984.
(62) Rezania, B.; Severin, N.; Talyzin, A. V.; Rabe, J. P. Hydration of Bilayered Graphene Oxide. *Nano Lett.* **2014**, *14*, 3993−3998.
(63) Meille, S. V.; Bruckner, S.; Porzio, W. $\gamma$-Isotactic Polypropylene. A Structure with Nonparallel Chain Axes. *Macromolecules* **1990**, *23*, 4114−4121.
(64) Gorrasi, G.; Tammaro, L.; Tortora, M.; Vittoria, V.; Kaempfer, D.; Reichert, P.; Mülhaupt, R. Transport Properties of Organic Vapors in Nanocomposites of Isotactic Polypropylene. *J. Polym. Sci., Part B: Polym. Phys.* **2003**, *41*, 1798−1805.
(65) Sinha Ray, S.; Okamoto, M. Polymer/Layered Silicate Nanocomposites: A Review From Preparation to Processing. *Prog. Polym. Sci.* **2003**, *28*, 1539−1641.
(66) Gau, V.; Ma, S.-C.; Wang, H.; Tsukuda, J.; Kibler, J.; Haake, D. A. Electrochemical Molecular Analysis without Nucleic Acid Amplification. *Methods* **2005**, *37*, 73−83.
(67) Park, M.-K.; Deng, S.; Advincula, R. C. pH-Sensitive Bipolar Ion-Permselective Ultrathin Films. *J. Am. Chem. Soc.* **2004**, *126*, 13723−13731.
(68) Motornov, M.; Kin Tam, T.; Pita, M.; Tokarev, I.; Katz, E.; Minko, S. Switchable Selectivity for Gating Ion Transport with Mixed Polyelectrolyte Brushes: Approaching 'Smart' Drug Delivery Systems. *Nanotechnology* **2009**, *20*, 434006.
(69) Hummers, W. S., Jr.; Offeman, R. E. Preparation of Graphitic Oxide. *J. Am. Chem. Soc.* **1958**, *80*, 1339−1339.
(70) Park, S.; Ruoff, R. S. Chemical Methods for the Production of Graphenes. *Nat. Nanotechnol.* **2009**, *4*, 217−224.
(71) Dreyer, D. R.; Park, S.; Bielawski, C. W.; Ruoff, R. S. The Chemistry of Graphene Oxide. *Chem. Soc. Rev.* **2010**, *39*, 228−240.
(72) Kang, J. H.; Kim, T.; Choi, J.; Park, J.; Kim, Y. S.; Chang, M. S.; Jung, H.; Park, K. T.; Yang, S. J.; Park, C. R. Hidden Second Oxidation Step of Hummers Method. *Chem. Mater.* **2016**, *28*, 756−764.
(73) Lee, T.; Min, S. H.; Gu, M.; Jung, Y. K.; Lee, W.; Lee, J. U.; Seong, D. G.; Kim, B.-S. Layer-by-Layer Assembly for Graphene-Based Multilayer Nanocomposites: Synthesis and Applications. *Chem. Mater.* **2015**, *27*, 3785−3796.


https://dx.doi.org/10.1021/acsami.9b20398
*ACS Appl. Mater. Interfaces* 2020, 12, 13116−13126